Foxi1 regulates multiple steps of mucociliary development and ionocyte specification through transcriptional and epigenetic mechanisms

Sarah Bowden[1,2,3,&], Magdalena Maria Brislinger-Engelhardt[1,2,4,&], Mona Hansen[1,4,&], Africa Temporal-Plo[1,2,3], Damian Weber[1,2], Sandra Hägele[1,2], Fabian Lorenz[2,5], Tim Litwin[2,5], Clemens Kreutz[2,5], Peter Walentek[1,2,3,4,#]

[1] Internal Medicine IV, Medical Center - University of Freiburg, Hugstetter Strasse 55, 79106 Freiburg, Germany.
[2] CIBSS Centre for Integrative Biological Signalling Studies, University of Freiburg, Schänzlestrasse 18, 79104 Freiburg, Germany.
[3] IMPRS-IEM International Max Planck Research School of Immunobiology, Epigenetics and Metabolism, Max Planck Institute of Immunobiology and Epigenetics, Stübeweg 51, 79108 Freiburg, Germany.
[4] SGBM Spemann Graduate School for Biology and Medicine, University of Freiburg, Albertstrasse 19A, 79104 Freiburg, Germany.
[5] IMBI Institute of Medical Biometry and Statistics, Medical Center - University of Freiburg, Stefan-Meier-Strasse 26, 70104, Freiburg, Germany.
[&] These authors contributed equally and are listed in alphabetical order.
[#] Corresponding author: peter.walentek@medizin.uni-freiburg.de

Key words:

Xenopus epidermis, development, mucociliary, ionocytes, multipotent progenitors

Abstract

Foxi1 is a master regulator of ionocytes (ISCs / INCs) across species and organs. Two subtypes of ISCs exist, and both α- and β-ISCs regulate pH- and ion-homeostasis in epithelia. Gain and loss of FOXI1 function are associated with human diseases, including Pendred syndrome, male infertility, renal acidosis and cancers. Foxi1 functions were predominantly studied in the context of ISC specification, however, reports indicate additional functions in early and ectodermal development. Here, we re-investigated the functions of Foxi1 in *Xenopus laevis* embryonic mucociliary epidermis development and found a novel function for Foxi1 in the generation of Notch-ligand expressing mucociliary multipotent progenitors (MPPs). We demonstrate that Foxi1 has multiple concentration-dependent functions: At low levels, Foxi1 confers ectodermal competence through transcriptional and epigenetic mechanisms, while at high levels, Foxi1 induces a multi-step process of ISC specification and differentiation. We further describe how *foxi1* expression is affected through auto- and Notch-regulation, how Ubp1 and Dmrt2 regulate ISC subtype differentiation, and how this developmental program affects Notch signaling as well as mucociliary patterning. Together, we reveal novel functions for Foxi1 in *Xenopus* mucociliary epidermis formation, relevant to our understanding of vertebrate development and human disease.

Introduction

The Forkhead-box transcription factor Foxi1 is a master regulator of ionocytes (ISCs) in the lung, kidney, inner ear and epididymis across vertebrates (Hulander et al., 2003; Pou Casellas et al., 2023). ISCs regulate ion homeostasis through the expression of an array of transmembrane solute carriers (e.g. Pendrin encoded by *slc26a4* and Anion exchanger 1 encoded by *slc4a1*) and pH-regulators (e.g. vacuolar (v)H^+ATPase encoded by *atp6* subunit genes and Carbonic anhydrase encoded by *ca* genes). α-ISCs and β-ISCs are subtypes with apical vs. basolateral vH^+ATPase localization and differential transporter expression of *slc26a4* and *slc4a1* (Quigley et al., 2011). In ISCs of the mammalian airway mucociliary epithelium, Foxi1 also regulates the expression of *cystic fibrosis transmembrane conductance regulator* (*CFTR*), thereby controlling chloride secretion and mucus properties (Montoro et al., 2018; Plasschaert et al., 2018; Scudieri et al., 2020). Mutations in *FOXI1* and its transcriptional target solute carriers cause Pendred syndrome and hearing loss, male infertility, and distal renal tubular acidosis (Blomqvist et al., 2004; Blomqvist et al., 2006; Hulander et al., 2003; Yang et al., 2007). In contrast, Foxi1 overexpression is found in cancer subtypes, e.g. in chromophore renal cell carcinoma (chRCC) and in pulmonary large cell carcinoma (LCC) (Lindgren et al., 2017; Simbolo et al., 2024; Skala et al., 2020; Yamada et al., 2022).

The *Xenopus* embryonic epidermis is a popular model for vertebrate mucociliary epithelia development and disease studies (Walentek and Quigley, 2017). It forms

Foxi1-dependent α-ISCs and β-ISCs as well as multiciliated cells (MCCs), secretory cells (small secretory cells (SSCs) and goblet cells) and basal stem cells, similar to the mammalian airway epithelium (Brooks and Wallingford, 2014; Haas et al., 2019; Hayes et al., 2007; Quigley et al., 2011; Walentek, 2022; Walentek et al., 2014). Knockdown of *foxi1* in *Xenopus* caused a loss of epidermal ISCs as expected, but also induced defective ciliation in MCCs suggesting potential Foxi1 functions in other cell types (Dubaissi and Papalopulu, 2011; Mir et al., 2007). Foxi1 plays additional early roles in *Xenopus* ectoderm development: In the blastula and gastrula, *foxi1* is initially activated throughout the entire ectoderm where it is required as a determinant counteracting vegetal mesendoderm-inducing factors (Mir et al., 2007; Suri et al., 2005). In neurula stages, Foxi1 is required for placode formation in the neural plate border and for the specification of ISCs in the epidermis (Dubaissi and Papalopulu, 2011; Maharana and Schlosser, 2018; Quigley et al., 2011).

How Foxi1 regulates different aspects of *Xenopus* mucociliary epidermis development from ectoderm to ISC-subtype specification, and how it could affect development of additional mucociliary epidermis cell types remains unresolved. Understanding the range of Foxi1 functions in this important model for mucociliary biology could provide additional information regarding unappreciated Foxi1 functions in development and human disease.

Here, we re-examined the roles of Foxi1 in *Xenopus* mucociliary epidermis development. We found that Foxi1 acts in a concentration-dependent manner: At low levels, Foxi1 marks multipotent mucociliary progenitors (MPPs) and establishes ectodermal identity, at least in part through regulation of chromatin accessibility. At high

levels, Foxi1 induces ISC specification and subtype differentiation through Ubp1 and Dmrt2. High Foxi1 levels are achieved by positive auto-regulation and inhibited by Notch signaling. In this work, we elucidate novel concentration-dependent Foxi1 transcriptional and epigenetic functions in mucociliary development and ISC specification.

Results

Specification and differentiation of ISCs is a multi-step process

Previous work has defined a core ISC gene set in the *X. laevis* mucociliary epidermis (Quigley and Kintner, 2017). We generated epidermal mucociliary organoids from animal cap explants and conducted bulk RNA-sequencing (RNA-seq) analysis of core ISCs gene expression during epidermis development (Brislinger-Engelhardt et al., 2023; Haas et al., 2019; Walentek, 2018). Z-scores of normalized counts (TPM) of ISC transcripts were clustered to reveal dynamic co-expression (**Fig. 1A**). Five clusters clearly separated along developmental time, with cluster I being the only set of genes displaying strong expression during very early and late developmental stages, but not during cell fate specification stages (st. 10-16). Cluster II contained *foxi1*, the Notch ligand *dll1* and the cell cycle regulator *gadd45g*. Cluster III contained *ca12* and the transcription factor *ubp1*, which was shown to induce ISC formation upon overexpression in the epidermis (Quigley et al., 2011). Cluster IV contained multiple transcription factors, including *tfcp2l1*, required for ISC formation in mouse kidney (Werth et al., 2017). Cluster V was dominated by *slc26a4* and *atp6*-subunit expression during later differentiation of ISCs (st. 20–32). These data indicated that ISCs develop using a multi-step process.

To validate the core ISC gene set, we used manipulations to deplete or enrich ISCs in mucociliary organoids and RNA-seq at the beginning of cell fate specification (st. 10), at the end of cell fate specification (st. 16), during maturation and intercalation of ISCs (st. 25), and in the mature epithelium (st. 32) (Walentek and Quigley, 2017). As previously described (Quigley et al., 2011), increased Notch signaling (Notch intracellular domain (*nicd*) mRNA injections) inhibited core ISC gene expression, while inhibition of Notch signaling (injection of dominant-negative suppressor of hairless/RBPJ (*suh-dbm*) mRNA) promoted core ISC gene expression (**Fig. S1A,B**). Inhibition of Notch signaling in combination with MCC inhibition (by co-injection of *dominant-negative mcidas* (*dn-mcidas*) mRNA (Stubbs et al., 2012)) further increased core ISC gene expression, reflecting stronger overproduction of ISCs. However, expression of *tfcp2l1*, *atp6v0d1.L* and *csta.L* were reduced in these conditions suggesting that they might be expressed more in MCCs than in ISCs (**Fig. S1C**). Notch repression of *foxi1* by *nicd* was substantial but not statistically significant (**Fig. S1A**), potentially reflecting a Notch-independent function of Foxi1.

We used single-cell RNA-seq (scRNA-seq) data from at late *Xenopus laevis* epidermis stages containing mature ISCs (Aztekin et al., 2019). These data confirmed high levels of *foxi1*, *ubp1* and *atp6*-subunit expression in both ISC subtypes, while *slc4a1* was specifically expressed in α-ISCs and *slc26a4* in β-ISCs, as previously described (**Fig. S1D**). Interestingly, the transcription factor *dmrt2* (cluster IV) was exclusively expressed by α-ISCs (**Fig. S1D**), and loss of kidney α-ISCs was recently reported in *Dmrt2* knockout mice (Wu et al., 2024).

To test if *foxi1*, *ubp1* and *dmrt2* contribute differentially to ISC-subtype formation, we knocked down each factor using morpholino oligonucleotides (MOs) and analyzed ISC marker expression in the mature epidermis at st. 30-32 by whole-mount *in situ* hybridization (WMISH). Knockdown of *foxi1* led to a loss of pan-ISC marker *atp6v1e1*, which could be rescued and expanded by co- and over-expression of *foxi1* mRNA, respectively (**Fig. 1B,C**). *foxi1* knockdown also strongly reduced expression of *ubp1*, *dmrt2*, *slc24a6* and *slc4a1* (**Fig. 1C,D**), indicating a loss of both ISC subtypes in the mucociliary epidermis. In contrast, knockdown of *ubp1* specifically reduced expression of the β-ISC marker *slc26a4*, while *dmrt2* loss lead to inhibition of α-ISC-specific *slc4a1* expression (**Fig. 1E-H**). Importantly, *ubp1* and *dmrt2* MOs did not abolish pan-ISC expressed *foxi1* and *atp6v1e1* (**Fig. 1E-H**).

Taken together, these data suggest that Foxi1 determines ISC fate commitment, while Ubp1 and Dmrt2 regulate ISC-subtype differentiation in a multi-step process.

Foxi1 has multiple concentration-dependent functions

In addition to ISC-specification, an earlier role for Foxi1 as ectodermal determinant during blastula stages in *Xenopus* was described (Suri et al., 2005). However, our experiments investigating ISC formation after *foxi1* MO did not indicate a loss of epidermal identity.

To confirm this, we injected *foxi1* MO together with membrane GFP to identify targeted cells, and analyzed cell type composition and morphology in the mature mucociliary epidermis at st. 32 by immunofluorescence (IF) confocal microscopy (Walentek, 2018).

As previously described, we also observed reduced ciliation in MCCs after *foxi1* knockdown (Dubaissi and Papalopulu, 2011) as well as strongly reduced ISC and increased MCC numbers, with little effect on secretory cell types (SSCs and goblet cells) or epidermal identity (**Fig. 2A**). This indicated that *foxi1* knockdown reduced Foxi1 levels enough to inhibit ISC specification, but not strong enough to prevent ectoderm specification.

Next, we caused stronger depletion of Foxi1 using higher doses of *foxi1* MO. This treatment induced delamination of cells in gastrula stage embryos (**Fig. S2A**), as previously described (Mir et al., 2007), and frequent formation of skin lesions at st. 32 that could be rescued by co-injection of *foxi1* mRNA (**Fig. 2B**).

This suggests that low levels of Foxi1 are sufficient for ectoderm identity, while high Foxi1 levels are required for ISC specification.

Foxi1 induces multipotent mucociliary progenitors

Next, we analyzed *foxi1* expression by WMISH. In early blastula/gastrula (st. 9/10) stages *foxi1* is expressed at low levels in patches throughout the prospective ectoderm, which start to resolve at st. 12 with individual cells strongly increasing *foxi1* expression by st. 16, resulting in a salt-and-pepper pattern of individual cells by st. 32, representing individual ISCs (**Fig. S2B**). Hence, *foxi1* seems to be initially expressed in more epidermal cells than just in developing ISCs. To test if *foxi1* is expressed broadly in epidermal multipotent mucociliary progenitors (MPPs), we generated a fluorescent

reporter (*foxi1::gfp-utrophin*) (**Fig. S2C,D**) using a previously characterized *foxi1* promoter fragment (Cha et al., 2012).

First, we injected embryos with *foxi1::gfp-utrophin* and analyzed reporter activity at st. 32 by IF. Indeed, GFP signals were detected in ISCs, MCCs and SSCs, and even some goblet cells expressed GFP at low levels (**Fig. 2C**). In contrast, a well-characterized Mcidas/Foxj1-regulated promoter construct (Tasca et al., 2021) driving mScarletI fluorescence (*α-tub::mscarletI*) was expressed predominantly in MCCs (**Fig. S3A,B**). Next, we confirmed that reporter expression dynamics resemble endogenous *foxi1* expression patterns during epidermis development using WMISH (**Fig. 2D, S3C**) and GFP expression by IF (**Fig. 2E, S4A**). Reporter-driven *gfp* transcripts were detected at st. 9 - 32, starting with non-epithelial low-level expression at st. 9/10, which increased by st. 12/16 in deep and superficial layer cells, and at st. 32 expression was found predominantly in epithelial layer cells (**Fig. 2D, S3C**). GFP-fluorescent cells were detected from st. 10 onwards, predominantly in deep layer cells, but also in some cells of the outer epithelial layer (**Fig. 2E, S4A**). During st. 12-16, an increasing number of cells became GFP(+), including intercalating differentiating cells (**Fig. 2E, S4A**). During st. 20-32, the number of GFP(+) cells decreased and fluorescent cells were progressively confined to the epithelial outer cell layer - however, basal positioned GFP(+) cells were detected even at st. 32 (**Fig. 2E, S4A**).

Together these data support the conclusion that *foxi1* is initially expressed in MPPs during mucociliary development.

Foxi1(+) multipotent progenitors express Notch ligands during cell fate specification

Dll1 expression was assigned to ISCs by Quigley and colleagues, similar to Foxi(+) cells in the zebrafish skin and mammalian kidney (Janicke et al., 2007; Mukherjee et al., 2020; Quigley and Kintner, 2017). This is supported by scRNA-seq data from *X. tropicalis* development (Briggs et al., 2018) showing that *dll1* is transiently enriched in differentiating ISCs (**Fig. S4B**). However, another study observed *dll1* expression overlapping with different cell markers during patterning stages in the *Xenopus* epidermis (Cibois et al., 2015). Our temporal expression analysis indicated that Cluster II contained very early ISC genes, including *foxi1* and *dll1*, likely representing the MPPs and early ISC differentiation stages (**Fig. 1A**), in line with both published observations.

To address if *dll1* (and *dlc*; Brislinger-Engelhardt et al., 2023) expression is part of the differentiation program across mucociliary cell types or specific to MPPs and early ISCs, we tested whether master transcription factors inducing cell types of the mucociliary epidermis were able to induce Notch ligands prematurely. We overexpressed *foxi1* for MPPs/ISCs, *mcidas* and *foxj1* for MCCs, *foxa1* for SSCs or *ΔN-tp63* for basal cells. Only *foxi1* robustly induced *dll1* and *dlc* (**Fig. 3A, S4C**), and conversely, depletion of Foxi1 prevented *dll1* expression during cell fate specification stages (**Fig. 3B**). These results suggested that *dll1* is expressed in *foxi1*(+) MPPs and terminated by cell fate induction of MCCs, SSCs and basal cells, but not in ISCs, which maintain *foxi1* expression.

This raised the question how *dll1* expression is terminated during ISC differentiation. The *X. tropicalis* scRNA-seq data revealed that *dll1* enrichment to ISCs is lost once

ubp1 is expressed (Briggs et al., 2018) (**Fig. S4B**). To test if Ubp1 terminates *dll1* expression, we knocked down *ubp1* and analyzed embryos at the end of cell fate specification (st. 16) by WMISH. *foxi1* was maintained and *dll1* expression was prolonged after loss of Ubp1 (**Fig. 3C**). Analysis of cell type composition at st. 32 by IF in *ubp1* morphants further revealed reduced MCC and SSC numbers as well as appearance of intercalating cells with ambiguous morphology, likely representing incompletely differentiated ISCs (**Fig. 3D**). These results demonstrated that manipulating *foxi1* and ISC differentiation leads to dysregulated Notch dynamics during mucociliary development, which can affect MCCs and other epidermal cell types.

Together, these data demonstrate that Notch ligands are expressed by *foxi1*(+) MPPs during mucociliary patterning, and that Ubp1-dependent differentiation of ISCs or induction of MCC, SSC and basal cell fates terminate Notch ligand expression.

Feedback- and auto-regulation during ISC specification

Feedback regulation of *dll1* by Notch signaling was suggested in *Xenopus* epidermis development (Deblandre et al., 1999). RNA-seq analysis of ligand and receptor expression after Notch manipulations confirmed that gain of Notch signaling suppresses *dll1*, while blocking Notch increases and prolongs *dll1* expression (**Fig. S1A,B**). Knockdown of *dll1* or *notch1* and subsequent analysis of cell type composition by IF at st. 32 revealed a strong increase in ISCs, which was reversed by co-injection of *nicd* (**Fig. S5A**), confirming that ISC specification is negatively regulated by Notch signaling through Dll1 and Notch1. Furthermore, unilateral knockdown of *dll1* by different (low to

high) MO concentrations, and analysis of cell type markers between the targeted and untargeted control side at st. 16/17 by WMISH confirmed that modifying Dll1 levels sufficed to affect all cell types (**Fig. S5B**). Together, these data indicate that MPPs, ligand production and ISC specification are negatively regulated by Notch feedback.

This raised the question how MPPs can achieve high *foxi1* expression levels required for specification of ISC fate and Ubp1-/Dmrt2-dependent differentiation of mature ISC subtypes. One potential mechanism for conferring robust cell fate decisions is positive auto-regulation, and Foxi1 could activate its own expression using core Foxi motifs previously identified in the *foxi1* promoter (Cha et al., 2012). To test this, we deleted a Foxi2 binding region (**Fig. S2C,D**) and analyzed reporter activity at st. 32, i.e. long after *foxi2* expression is terminated. This strongly decreased reporter activity (**Fig. 4A**), suggesting that core Foxi motifs are also used by Foxi1 to maintain its expression through auto-regulation.

To verify that Foxi1 can also activate its own promoter without contributions from Foxi2, we injected *foxi1::gfp-utrophin* vegetally to target the prospective mesendoderm, which lacks maternally deposited *foxi2* (Cha et al., 2012). Analysis of reporter-only injected cells (marked by membrane RFP) in hemisected embryos at st. 11 showed no reporter activity in endodermal cells, while co-injection of *foxi1* mRNA led to ectopic activation of the reporter (**Fig 4B**).

In summary, Foxi1 induces first Dll1-expressing MPPs, which increase Notch levels during cell fate specification stages and terminates ISC production. Progenitors experiencing low Notch levels activate high *foxi1* expression through auto-regulation to induce ISC fate, and *dll1* expression is terminated in differentiating ISCs by Ubp1.

Foxi1 regulates genome accessibility in the epidermis

We wondered how early Foxi1 expression could have such a profound impact on ectodermal development and formation of mucociliary MPPs given that it is expressed at low levels. Besides its effects counteracting mesendoderm induction through transcriptional activation of ectodermal genes in early *Xenopus* embryos (Suri et al., 2005) Foxi1 has been shown to remain bound to condensed chromatin during mitosis, to remodel nucleosome structure and to alter the transcriptional ground state of cells in zebrafish embryos (Yan et al., 2006). This suggested a pioneer-like function for Foxi1.

To test if Foxi1 affects chromatin state and genomic accessibility in *Xenopus* epidermal development, we performed assays for transposase-accessible chromatin with sequencing (ATAC-seq) on st. 10 control epidermal organoids and organoids after knockdown of *foxi1*. This revealed a dramatic reduction in accessible chromatin regions after loss of Foxi1 (control: 311,328, *foxi1*MO: 146,640) (**Fig.5A**,**B**). In Foxi1-depleted organoids, 53.7% of accessible regions (169,077 peaks) were lost, 45.2% were maintained (142,251 peaks), and 1.1% were gained (4,389 peaks) (**Fig. 5B**). Next, we investigated which transcription factor binding motifs were enriched in regions lost, maintained or gained after *foxi1* MO. We found that motifs for factors with known functions in *Xenopus* ectodermal development were enriched in regions that lost accessibility after *foxi1* knockdown: e.g. Tfap2a and Tfap2c, Hic1, Rbfox2, Zac1 that regulate neural and neural crest formation as well as Tp63, which regulates epidermal basal stem cells, and Pitx1, required for cement gland formation (**Fig. 5C**) (Giudetti et al., 2014; Luo et al., 2005; Ma et al., 2007; Ray and Chang, 2020; Schweickert et al.,

2001; Zhang et al., 2006). In contrast, regions that remained open were enriched for mesendodermal transcription factors (e.g. Gata6, Tbxt, MyoD), and regions that gained in accessibility were enriched in pluripotency factors (e.g. Brn1, Oct4) (**Fig. 5C**) (Afouda et al., 2005; Hopwood et al., 1989; Jerabek et al., 2014; Mistri et al., 2015; Smith et al., 1991). Together, these data support a function for Foxi1 in regulating accessible chromatin state during ectodermal development in *Xenopus*.

Finally, we wondered how loss of Foxi1 affects chromatin accessibility in regions harboring important genes for mucociliary epidermis development. First, we inspected a region around the *krt12.4* (epidermal keratin) gene on chromosome 9/10.S, which revealed strongly reduced accessibility and indicated a loss of epidermal competence (**Fig. 5D**) (Wills et al., 2010). Next, we inspected genomic loci containing genes associated with MPPs (*dll1.L*), ISCs (*ubp1.L* and *dmrt2.S*), and mucociliary development (*foxj1.L* and *tp63.L*) (Deblandre et al., 1999; Haas et al., 2019; Quigley and Kintner, 2017; Quigley et al., 2011). In all cases, we found reduced accessibility (**Fig. 5D, Fig. S6A-D**). Together, these data support a broad function for Foxi1 in regulating ectodermal and mucociliary developmental potential.

In conclusion, Foxi1 regulates chromatin accessibility required for ectoderm development and mucociliary epidermis patterning. This provides an additional explanation as to how Foxi1 acts as an ectodermal determinant in early *Xenopus* development.

Discussion

This work revealed that Foxi1 regulates multiple crucial steps during *Xenopus* mucociliary epidermis development through transcriptional and epigenetic mechanisms. Initially, low-level *foxi1* expression is activated in the prospective ectoderm by maternally deposited *foxi2* (Cha et al., 2012). This low-level expression is required to regulate chromatin accessibility for pro-ectodermal transcription factors (e.g. Tfap2a/c), mucociliary regulators (e.g. Tp63) as well as mediators of thyroid hormone, retinoic acid and TGFβ signaling (e.g. Thrb, Rar-a, Smad4) that were described to regulate ectodermal development (Cibois et al., 2015; Edri et al., 2023; Haas et al., 2019; Hoffman et al., 2007; Tasca et al., 2021). Since baseline *foxi1* expression is Foxi2- but not Notch-dependent, Notch over-activation does not alter ectodermal identity in line with previous reports (Cha et al., 2012; Deblandre et al., 1999).

Furthermore, our data support previous findings that loss of Foxi1 leads to acquisition of mesendodermal fates, as loci enriched for pro-mesendodermal transcription factors (e.g. Gata6, Tbxt, MyoD) remain accessible in the absence of Foxi1 (Afouda et al., 2005; Hopwood et al., 1989; Smith et al., 1991). It is attractive to speculate that this is possible, because multiple transcription factors enriched in the maintained fraction of peaks (e.g. Gata and Sox family members) are known factors with pioneer activity (Hou et al., 2017; Tremblay et al., 2018), which could compensate for the loss of Foxi1.

After inducing ectodermal identity at low levels, Foxi1 then further increases its own expression through auto-regulation in mucociliary multipotent progenitors (MPPs), inducing Notch ligand expression (*dll1* and *dlc*) required for Notch-mediated mucociliary cell fate decisions into ISCs, MCCs, secretory cells and basal stem cells (Brislinger-Engelhardt et al., 2023). MPPs not exposed to elevated Notch levels further increase

foxi1 expression through auto-regulation, and high levels of Foxi1 induce ISC fate, in line with the known role of Foxi1 as master transcription factor for ionocytes across vertebrate tissues (Pou Casellas et al., 2023).

ISC subtype selection and differentiation is a multi-step process. In the *Xenopus* epidermis, Ubp1 is expressed first in both ISC subtypes, which terminates Notch ligand expression in differentiating ISCs. Ubp1 drives differentiation of β-ISCs, while Dmrt2 drives α-ISC differentiation. Interestingly, Dmrt2 has recently been shown to be required for α-ISCs in the mouse kidney, while not Ubp1, but the related grainyhead-like transcription factor Tfcp2l1 is employed in mammalian kidney β-ISCs (Quigley et al., 2011; Werth et al., 2017; Wu et al., 2024). This could explain why Dll1 expression is terminated in *Xenopus* epidermal ISCs, but remains active in mammalian kidney ISCs (also called INCs) (Mukherjee et al., 2020; Werth et al., 2017).

Similarly to Ubp1, our results suggest that master transcription factors for other mucociliary epidermal cell types also terminate Dll1/Dlc ligand expression in MPPs. Together, this system provides a robust Notch feedback-regulated developmental program for mucociliary epidermis development, with Foxi1 as a central player that acts through transcriptional and epigenetic mechanisms.

Finally, our finding that Foxi1 drives an MPP state during mucociliary epidermis development could serve as a starting point to better understand the role of Foxi1 in certain cancers, e.g. chromophore renal cell carcinoma (chRCC) and in pulmonary large cell carcinoma (LCC), both highly associated with Foxi1 activity (Lindgren et al., 2017; Simbolo et al., 2024; Skala et al., 2020; Yamada et al., 2022).

References

Afouda, B.A., A. Ciau-Uitz, and R. Patient. 2005. GATA4, 5 and 6 mediate TGFbeta maintenance of endodermal gene expression in Xenopus embryos. *Development*. 132:763-774.

Aztekin, C., T.W. Hiscock, J.C. Marioni, J.B. Gurdon, B.D. Simons, and J. Jullien. 2019. Identification of a regeneration-organizing cell in the Xenopus tail. *Science*. 364:653-658.

Blomqvist, S.R., H. Vidarsson, S. Fitzgerald, B.R. Johansson, A. Ollerstam, R. Brown, A.E. Persson, G.G. Bergstrom, and S. Enerback. 2004. Distal renal tubular acidosis in mice that lack the forkhead transcription factor Foxi1. *J Clin Invest*. 113:1560-1570.

Blomqvist, S.R., H. Vidarsson, O. Soder, and S. Enerback. 2006. Epididymal expression of the forkhead transcription factor Foxi1 is required for male fertility. *EMBO J*. 25:4131-4141.

Briggs, J.A., C. Weinreb, D.E. Wagner, S. Megason, L. Peshkin, M.W. Kirschner, and A.M. Klein. 2018. The dynamics of gene expression in vertebrate embryogenesis at single-cell resolution. *Science*. 360.

Brislinger-Engelhardt, M.M., F. Lorenz, M. Haas, S. Bowden, A. Tasca, C. Kreutz, and P. Walentek. 2023. Temporal Notch signaling regulates mucociliary cell fates through Hes-mediated competitive de-repression. *bioRxiv*.

Brooks, E.R., and J.B. Wallingford. 2014. Multiciliated cells. *Curr Biol*. 24:R973-982.

Buenrostro, J.D., P.G. Giresi, L.C. Zaba, H.Y. Chang, and W.J. Greenleaf. 2013. Transposition of native chromatin for fast and sensitive epigenomic profiling of open chromatin, DNA-binding proteins and nucleosome position. *Nat Methods*. 10:1213-1218.

Cha, S.W., M. McAdams, J. Kormish, C. Wylie, and M. Kofron. 2012. Foxi2 is an animally localized maternal mRNA in Xenopus, and an activator of the zygotic ectoderm activator Foxi1e. *PLoS One*. 7:e41782.

Cibois, M., G. Luxardi, B. Chevalier, V. Thome, O. Mercey, L.E. Zaragosi, P. Barbry, A. Pasini, B. Marcet, and L. Kodjabachian. 2015. BMP signalling controls the construction of vertebrate mucociliary epithelia. *Development*. 142:2352-2363.

Community, T.G. 2024. The Galaxy platform for accessible, reproducible, and collaborative data analyses: 2024 update. *Nucleic Acids Research*. 52:W83-W94.

Danecek, P., J.K. Bonfield, J. Liddle, J. Marshall, V. Ohan, M.O. Pollard, A. Whitwham, T. Keane, S.A. McCarthy, R.M. Davies, and H. Li. 2021. Twelve years of SAMtools and BCFtools. *GigaScience*. 10.

406 Deblandre, G.A., D.A. Wettstein, N. Koyano-Nakagawa, and C. Kintner. 1999. A two-step mechanism
407 generates the spacing pattern of the ciliated cells in the skin of Xenopus embryos. *Development*.
408 126:4715-4728.
409 Dubaissi, E., and N. Papalopulu. 2011. Embryonic frog epidermis: a model for the study of cell-cell
410 interactions in the development of mucociliary disease. *Dis Model Mech*. 4:179-192.
411 Dubaissi, E., K. Rousseau, R. Lea, X. Soto, S. Nardeosingh, A. Schweickert, E. Amaya, D.J. Thornton, and N.
412 Papalopulu. 2014. A secretory cell type develops alongside multiciliated cells, ionocytes and
413 goblet cells, and provides a protective, anti-infective function in the frog embryonic mucociliary
414 epidermis. *Development*. 141:1514-1525.
415 Edri, T., D. Cohen, Y. Shabtai, and A. Fainsod. 2023. Alcohol induces neural tube defects by reducing
416 retinoic acid signaling and promoting neural plate expansion. *Front Cell Dev Biol*. 11:1282273.
417 Esmaeili, M., S.A. Blythe, J.W. Tobias, K. Zhang, J. Yang, and P.S. Klein. 2020. Chromatin accessibility and
418 histone acetylation in the regulation of competence in early development. *Dev Biol*. 462:20-35.
419 Feng, J., T. Liu, B. Qin, Y. Zhang, and X.S. Liu. 2012. Identifying ChIP-seq enrichment using MACS. *Nat*
420 *Protoc*. 7:1728-1740.
421 Fisher, M., C. James-Zorn, V. Ponferrada, A.J. Bell, N. Sundararaj, E. Segerdell, P. Chaturvedi, N. Bayyari,
422 S. Chu, T. Pells, V. Lotay, S. Agalakov, D.Z. Wang, B.I. Arshinoff, S. Foley, K. Karimi, P.D. Vize, and
423 A.M. Zorn. 2023. Xenbase: key features and resources of the Xenopus model organism
424 knowledgebase. *Genetics*. 224.
425 Giudetti, G., M. Giannaccini, D. Biasci, S. Mariotti, A. Degl'innocenti, M. Perrotta, G. Barsacchi, and M.
426 Andreazzoli. 2014. Characterization of the Rx1-dependent transcriptome during early retinal
427 development. *Dev Dyn*. 243:1352-1361.
428 Haas, M., J.L. Gomez Vazquez, D.l. Sun, H.T. Tran, M. Brislinger, A. Tasca, O. Shomroni, K. Vleminckx, and
429 P. Walentek. 2019. DeltaN-Tp63 Mediates Wnt/beta-Catenin-Induced Inhibition of
430 Differentiation in Basal Stem Cells of Mucociliary Epithelia. *Cell Rep*. 28:3338-3352 e3336.
431 Harland, R.M. 1991. In situ hybridization: an improved whole-mount method for Xenopus embryos.
432 *Methods Cell Biol*. 36:685-695.
433 Hayes, J.M., S.K. Kim, P.B. Abitua, T.J. Park, E.R. Herrington, A. Kitayama, M.W. Grow, N. Ueno, and J.B.
434 Wallingford. 2007. Identification of novel ciliogenesis factors using a new in vivo model for
435 mucociliary epithelial development. *Dev Biol*. 312:115-130.
436 Heinz, S., C. Benner, N. Spann, E. Bertolino, Y.C. Lin, P. Laslo, J.X. Cheng, C. Murre, H. Singh, and C.K.
437 Glass. 2010. Simple combinations of lineage-determining transcription factors prime cis-
438 regulatory elements required for macrophage and B cell identities. *Mol Cell*. 38:576-589.
439 Hoffman, T.L., A.L. Javier, S.A. Campeau, R.D. Knight, and T.F. Schilling. 2007. Tfap2 transcription factors
440 in zebrafish neural crest development and ectodermal evolution. *J Exp Zool B Mol Dev Evol*.
441 308:679-691.
442 Hopwood, N.D., A. Pluck, and J.B. Gurdon. 1989. MyoD expression in the forming somites is an early
443 response to mesoderm induction in Xenopus embryos. *Embo j*. 8:3409-3417.
444 Hou, L., Y. Srivastava, and R. Jauch. 2017. Molecular basis for the genome engagement by Sox proteins.
445 *Semin Cell Dev Biol*. 63:2-12.
446 Hulander, M., A.E. Kiernan, S.R. Blomqvist, P. Carlsson, E.J. Samuelsson, B.R. Johansson, K.P. Steel, and S.
447 Enerback. 2003. Lack of pendrin expression leads to deafness and expansion of the
448 endolymphatic compartment in inner ears of Foxi1 null mutant mice. *Development*. 130:2013-
449 2025.
450 Janicke, M., T.J. Carney, and M. Hammerschmidt. 2007. Foxi3 transcription factors and Notch signaling
451 control the formation of skin ionocytes from epidermal precursors of the zebrafish embryo. *Dev*
452 *Biol*. 307:258-271.

453 Jerabek, S., F. Merino, H.R. Schöler, and V. Cojocaru. 2014. OCT4: dynamic DNA binding pioneers stem
454 cell pluripotency. *Biochim Biophys Acta*. 1839:138-154.
455 Lindgren, D., P. Eriksson, K. Krawczyk, H. Nilsson, J. Hansson, S. Veerla, J. Sjolund, M. Hoglund, M.E.
456 Johansson, and H. Axelson. 2017. Cell-Type-Specific Gene Programs of the Normal Human
457 Nephron Define Kidney Cancer Subtypes. *Cell Rep*. 20:1476-1489.
458 Luo, T., Y. Zhang, D. Khadka, J. Rangarajan, K.W. Cho, and T.D. Sargent. 2005. Regulatory targets for
459 transcription factor AP2 in Xenopus embryos. *Dev Growth Differ*. 47:403-413.
460 Ma, L., J.C. Hocking, C.L. Hehr, C. Schuurmans, and S. McFarlane. 2007. Zac1 promotes a Müller glial cell
461 fate and interferes with retinal ganglion cell differentiation in Xenopus retina. *Dev Dyn*. 236:192-
462 202.
463 Maharana, S.K., and G. Schlosser. 2018. A gene regulatory network underlying the formation of pre-
464 placodal ectoderm in Xenopus laevis. *BMC Biol*. 16:79.
465 Mir, A., M. Kofron, A.M. Zorn, M. Bajzer, M. Haque, J. Heasman, and C.C. Wylie. 2007. Foxl1e activates
466 ectoderm formation and controls cell position in the Xenopus blastula. *Development*. 134:779-
467 788.
468 Mistri, T.K., A.G. Devasia, L.T. Chu, W.P. Ng, F. Halbritter, D. Colby, B. Martynoga, S.R. Tomlinson, I.
469 Chambers, P. Robson, and T. Wohland. 2015. Selective influence of Sox2 on POU transcription
470 factor binding in embryonic and neural stem cells. *EMBO Rep*. 16:1177-1191.
471 Montoro, D.T., A.L. Haber, M. Biton, V. Vinarsky, B. Lin, S.E. Birket, F. Yuan, S. Chen, H.M. Leung, J.
472 Villoria, N. Rogel, G. Burgin, A.M. Tsankov, A. Waghray, M. Slyper, J. Waldman, L. Nguyen, D.
473 Dionne, O. Rozenblatt-Rosen, P.R. Tata, H. Mou, M. Shivaraju, H. Bihler, M. Mense, G.J. Tearney,
474 S.M. Rowe, J.F. Engelhardt, A. Regev, and J. Rajagopal. 2018. A revised airway epithelial
475 hierarchy includes CFTR-expressing ionocytes. *Nature*. 560:319-324.
476 Mukherjee, M., J. DeRiso, M. Janga, E. Fogarty, and K. Surendran. 2020. Foxi1 inactivation rescues loss of
477 principal cell fate selection in Hes1-deficient kidneys but does not ensure maintenance of
478 principal cell gene expression. *Dev Biol*. 466:1-11.
479 Plasschaert, L.W., R. Zilionis, R. Choo-Wing, V. Savova, J. Knehr, G. Roma, A.M. Klein, and A.B. Jaffe.
480 2018. A single-cell atlas of the airway epithelium reveals the CFTR-rich pulmonary ionocyte.
481 *Nature*. 560:377-381.
482 Pou Casellas, C., C. Pleguezuelos-Manzano, M.B. Rookmaaker, M.C. Verhaar, and H. Clevers. 2023.
483 Transcriptomic profile comparison reveals conservation of ionocytes across multiple organs. *Sci*
484 *Rep*. 13:3516.
485 Quigley, I.K., and C. Kintner. 2017. Rfx2 Stabilizes Foxj1 Binding at Chromatin Loops to Enable
486 Multiciliated Cell Gene Expression. *PLoS Genet*. 13:e1006538.
487 Quigley, I.K., J.L. Stubbs, and C. Kintner. 2011. Specification of ion transport cells in the Xenopus larval
488 skin. *Development*. 138:705-714.
489 Ramírez, F., D.P. Ryan, B. Grüning, V. Bhardwaj, F. Kilpert, A.S. Richter, S. Heyne, F. Dündar, and T.
490 Manke. 2016. deepTools2: a next generation web server for deep-sequencing data analysis.
491 *Nucleic Acids Research*. 44:W160-W165.
492 Ray, H., and C. Chang. 2020. The transcription factor Hypermethylated in Cancer 1 (Hic1) regulates
493 neural crest migration via interaction with Wnt signaling. *Dev Biol*. 463:169-181.
494 Schindelin, J., I. Arganda-Carreras, E. Frise, V. Kaynig, M. Longair, T. Pietzsch, S. Preibisch, C. Rueden, S.
495 Saalfeld, B. Schmid, J.Y. Tinevez, D.J. White, V. Hartenstein, K. Eliceiri, P. Tomancak, and A.
496 Cardona. 2012. Fiji: an open-source platform for biological-image analysis. *Nat Methods*. 9:676-
497 682.
498 Schweickert, A., H. Steinbeisser, and M. Blum. 2001. Differential gene expression of Xenopus Pitx1,
499 Pitx2b and Pitx2c during cement gland, stomodeum and pituitary development. *Mech Dev*.
500 107:191-194.

501 Scudieri, P., I. Musante, A. Venturini, D. Guidone, M. Genovese, F. Cresta, E. Caci, A. Palleschi, M. Poeta,
502 F. Santamaria, F. Ciciriello, V. Lucidi, and L.J.V. Galietta. 2020. Ionocytes and CFTR Chloride
503 Channel Expression in Normal and Cystic Fibrosis Nasal and Bronchial Epithelial Cells. *Cells*. 9.
504 Simbolo, M., G. Centonze, A. Gkountakos, V. Monti, P. Maisonneuve, S. Golovco, G. Sabella, A. Del
505 Gobbo, S. Gobbo, S. Ferrero, A. Fabbri, C. Pardo, G. Garzone, N. Prinzi, S. Pusceddu, A. Testi, L.
506 Rolli, A. Mangogna, L. Bercich, M.R. Benvenuti, E. Bria, S. Pilotto, A. Berruti, U. Pastorino, C.
507 Capella, M. Infante, M. Milella, A. Scarpa, and M. Milione. 2024. Characterization of two
508 transcriptomic subtypes of marker-null large cell carcinoma of the lung suggests different origin
509 and potential new therapeutic perspectives. *Virchows Arch*. 484:777-788.
510 Sive, H.L., R.M. Grainger, and R.M. Harland. 2007a. Animal Cap Isolation from Xenopus laevis. *CSH*
511 *Protoc*. 2007:pdb.prot4744.
512 Sive, H.L., R.M. Grainger, and R.M. Harland. 2007b. Xenopus laevis In Vitro Fertilization and Natural
513 Mating Methods. *CSH Protoc*. 2007:pdb.prot4737.
514 Sive, H.L., R.M. Grainger, and R.M. Harland. 2010. Microinjection of Xenopus embryos. *Cold Spring Harb*
515 *Protoc*. 2010:pdb.ip81.
516 Skala, S.L., X. Wang, Y. Zhang, R. Mannan, L. Wang, S.P. Narayanan, P. Vats, F. Su, J. Chen, X. Cao, J.
517 Siddiqui, P. Argani, M.P. Cieslik, T.J. Giordano, A.M. Chinnaiyan, S.M. Dhanasekaran, and R.
518 Mehra. 2020. Next-generation RNA Sequencing-based Biomarker Characterization of
519 Chromophobe Renal Cell Carcinoma and Related Oncocytic Neoplasms. *Eur Urol*. 78:63-74.
520 Smith, J.C., B.M. Price, J.B. Green, D. Weigel, and B.G. Herrmann. 1991. Expression of a Xenopus
521 homolog of Brachyury (T) is an immediate-early response to mesoderm induction. *Cell*. 67:79-
522 87.
523 Stubbs, J.L., I. Oishi, J.C. Izpisúa Belmonte, and C. Kintner. 2008. The forkhead protein Foxj1 specifies
524 node-like cilia in Xenopus and zebrafish embryos. *Nat Genet*. 40:1454-1460.
525 Stubbs, J.L., E.K. Vladar, J.D. Axelrod, and C. Kintner. 2012. Multicilin promotes centriole assembly and
526 ciliogenesis during multiciliate cell differentiation. *Nat Cell Biol*. 14:140-147.
527 Suri, C., T. Haremaki, and D.C. Weinstein. 2005. Xema, a foxi-class gene expressed in the gastrula stage
528 Xenopus ectoderm, is required for the suppression of mesendoderm. *Development*. 132:2733-
529 2742.
530 Tasca, A., M. Helmstadter, M.M. Brislinger, M. Haas, B. Mitchell, and P. Walentek. 2021. Notch signaling
531 induces either apoptosis or cell fate change in multiciliated cells during mucociliary tissue
532 remodeling. *Dev Cell*. 56:525-539 e526.
533 Tremblay, M., O. Sanchez-Ferras, and M. Bouchard. 2018. GATA transcription factors in development
534 and disease. *Development*. 145.
535 Walentek, P. 2018. Manipulating and Analyzing Cell Type Composition of the Xenopus Mucociliary
536 Epidermis. *Methods Mol Biol*. 1865:251-263.
537 Walentek, P. 2022. Signaling Control of Mucociliary Epithelia: Stem Cells, Cell Fates, and the Plasticity of
538 Cell Identity in Development and Disease. *Cells Tissues Organs*. 211:736-753.
539 Walentek, P., T. Beyer, C. Hagenlocher, C. Muller, K. Feistel, A. Schweickert, R.M. Harland, and M. Blum.
540 2015. ATP4a is required for development and function of the Xenopus mucociliary epidermis - a
541 potential model to study proton pump inhibitor-associated pneumonia. *Dev Biol*. 408:292-304.
542 Walentek, P., T. Beyer, T. Thumberger, A. Schweickert, and M. Blum. 2012. ATP4a is required for Wnt-
543 dependent Foxj1 expression and leftward flow in Xenopus left-right development. *Cell Rep*.
544 1:516-527.
545 Walentek, P., S. Bogusch, T. Thumberger, P. Vick, E. Dubaissi, T. Beyer, M. Blum, and A. Schweickert.
546 2014. A novel serotonin-secreting cell type regulates ciliary motility in the mucociliary epidermis
547 of Xenopus tadpoles. *Development*. 141:1526-1533.

548 Walentek, P., and I.K. Quigley. 2017. What we can learn from a tadpole about ciliopathies and airway
549 diseases: Using systems biology in Xenopus to study cilia and mucociliary epithelia. *Genesis*. 55.
550 Werth, M., K.M. Schmidt-Ott, T. Leete, A. Qiu, C. Hinze, M. Viltard, N. Paragas, C.J. Shawber, W. Yu, P.
551 Lee, X. Chen, A. Sarkar, W. Mu, A. Rittenberg, C.S. Lin, J. Kitajewski, Q. Al-Awqati, and J. Barasch.
552 2017. Transcription factor TFCP2L1 patterns cells in the mouse kidney collecting ducts. *Elife*. 6.
553 Wills, A.E., V.M. Choi, M.J. Bennett, M.K. Khokha, and R.M. Harland. 2010. BMP antagonists and FGF
554 signaling contribute to different domains of the neural plate in Xenopus. *Dev Biol*. 337:335-350.
555 Wu, S.T., Y. Feng, R. Song, Y. Qi, L. Li, D. Lu, Y. Wang, W. Wu, A. Morgan, X. Wang, Y. Xia, R. Liu, S.I.
556 Alexander, J. Wong, Y. Zhang, and X. Zheng. 2024. Foxp1 Is Required for Renal Intercalated Cell
557 Differentiation and Acid-Base Regulation. *J Am Soc Nephrol*. 35:533-548.
558 Yamada, Y., D. Belharazem-Vitacolonnna, H. Bohnenberger, C. Weiss, N. Matsui, M. Kriegsmann, K.
559 Kriegsmann, P. Sinn, K. Simon-Keller, G. Hamilton, T. Graeter, G. Preissler, G. Ott, S. Scholch, N.
560 Nakajima, A. Yoshizawa, H. Haga, H. Date, R.K. Thomas, I. Petrini, G. Giaccone, P. Strobel, and A.
561 Marx. 2022. Pulmonary cancers across different histotypes share hybrid tuft cell/ionocyte-like
562 molecular features and potentially druggable vulnerabilities. *Cell Death Dis*. 13:979.
563 Yan, J., L. Xu, G. Crawford, Z. Wang, and S.M. Burgess. 2006. The forkhead transcription factor Foxl1
564 remains bound to condensed mitotic chromosomes and stably remodels chromatin structure.
565 *Mol Cell Biol*. 26:155-168.
566 Yang, T., H. Vidarsson, S. Rodrigo-Blomqvist, S.S. Rosengren, S. Enerback, and R.J. Smith. 2007.
567 Transcriptional control of SLC26A4 is involved in Pendred syndrome and nonsyndromic
568 enlargement of vestibular aqueduct (DFNB4). *Am J Hum Genet*. 80:1055-1063.
569 Zhang, Y., T. Luo, and T.D. Sargent. 2006. Expression of TFAP2beta and TFAP2gamma genes in Xenopus
570 laevis. *Gene Expr Patterns*. 6:589-595.

571

572 **Acknowledgments:**

573 We thank: S. Schefold and A. Andricek for expert technical help; L. Kodjabachian and
574 team, T. Manke and W. Deboutte, T. Kwon for support and discussions; Xenbase,
575 EXRC for Xenopus resources; Light Imaging Center Freiburg, BiMiC and Aqua Core for
576 microscope/animal resources; B. Grüning and the Freiburg Galaxy Team for
577 bioinformatics platform and support. This study was supported by the Deutsche
578 Forschungsgemeinschaft (DFG) under the Emmy Noether and Heisenberg
579 Programmes (grant WA3365/2-1 and WA3365/5-1), by DFG SFB1453 NephGen
580 (Project ID 431984000), by DFG/ANR grant WA3365/4-1, and by the NHLBI through a
581 Pathway to Independence Award (K99HL127275) to PW; and under Germany's
582 Excellence Strategy (CIBSS – EXC-2189 – Project ID 390939984) to PW and CK.

583

584 **Author contribution:**

585 SB: epigenetics; MMBE: cell fates and Notch; MOH: reporter studies; ATP, DW, SH,
586 PW: experimental support; SB, MMBE, MOH, PW: experimental design, planning,
587 analysis and interpretation of data; FL, TL, CK: crucial discussion and mathematical
588 modeling; PW, SB: bioinformatics. PW: study design and supervision, coordinating

collaborative work, manuscript preparation with input from all authors. SB, MMBE, MOH contributed equally and can list themselves as first co-first authors.

Material and Mathods:

Animal experiments:

Wild-type *Xenopus laevis* were obtained from the European Xenopus Resource Centre (EXRC) at University of Portsmouth, School of Biological Sciences, UK, or Xenopus 1, USA. Frog maintenance and care was conducted according to standard procedures in the AquaCore facility, University Freiburg, Medical Center (RI_00544) and based on recommendations provided by the international Xenopus community resource centers NXR (RRID:SCR_013731) and EXRC as well as by Xenbase (http://www.xenbase.org/, RRID:SCR_003280)(Fisher et al., 2023). This work was done in compliance with German animal protection laws and was approved under Registrier-Nr. G-18/76 and G-22/43 by the state of Baden-Württemberg.

Data availability:

NGS datasets are available via NCBI GEO, ATAC-seq datasets (# pending), mRNA-seq datasets were generated in previous studies (GSE130448, GSE215373, GSE215419, GSE262944)(Brislinger-Engelhardt et al., 2023; Haas et al., 2019). Imaging and quantification data are available to the scientific community upon request to peter.walentek@medizin.uni-freiburg.de.

Manipulation of *Xenopus* Embryos:

X. laevis eggs were collected and in vitro-fertilized, then cultured and microinjected by standard procedures (Sive et al., 2007b; Sive et al., 2010). Embryos were injected with Morpholino oligonucleotides (MOs, Gene Tools), mRNAs or plasmid DNA at two-cell to eight-cell stage using a PicoSpritzer setup in 1/3x Modified Frog Ringer's solution (MR)

with 2.5% Ficoll PM 400 (GE Healthcare, #17-0300-50), and were transferred after injection into 1/3x MR containing Gentamycin. Drop size was calibrated to about 7–8nL per injection.

Embryos injected with hormone-inducible constructs of (GFP-ΔN-tp63-GR and MCI-GR) (Haas et al., 2019; Stubbs et al., 2012) were treated with 10µM Dexamethasone (Sigma-Aldrich/Merck #D4902) in ethanol from eight-cell stage until fixation. Ultrapure Ethanol (NeoFroxx #LC-8657.3) was used as vehicle control.

Morpholino oligonucleotides (MOs) were obtained from Gene Tools targeting *dll1*, *dmrt2*, *foxi1*, *notch1* and *ubp1* and were used at doses as indicated in the list below.

mRNAs encoding *nicd (*100 ng/µl*)* (Deblandre et al., 1999), *foxi1 (25-100*ng/µl*)* (this study using primers listed below into pCS107), *mcidas* (100ng/µl) (Stubbs et al., 2012), *foxj1* (100ng/µl) (Stubbs et al., 2008), *foxa1* (100ng/µl) (Dubaissi et al., 2014; Walentek et al., 2014), *ΔN-tp63* (100ng/µl) (Haas et al., 2019) were injected together with *membrane-gfp* or *membrane-rfp* (at 50ng/µL) or *h2b-rfp* (at 30ng/µL) as lineage tracers. All mRNAs were prepared using the mMessage Machine kit using Sp6 (Invitrogen #AM1340) supplemented with RNAse Inhibitor (Promega #N251B).

The *foxi1::gfp-utrophin*, *foxi1Δ1::gfp-utrophin* and *a-tub::mscarletI* plasmids were purified using the Pure Yield midiprep kit (Promega #A2492) and injected at 5 ng/µl.

Morpholino Sequences and doses:

Name	**Sequence**	**Concentration Range**
dll1.L MO	5'-CCCATGTTGTCTGATATGCGATTG-3'	0.5-2 pmol
dll1.S MO	5'-AGGCACTGCTGTCCCATGTTG-3'	0.5-2 pmol
dmrt2 MO	5'-GTGCCTTCATCTCGTACATCTCCAG-3'	1.5 pmol
foxi1MO	5'-GTGCTTGTGGATCAAATGCACTCAT-3'	1.5-3 pmol
notch1 MO	5'-GCACAGCCAGCCCTATCCGATCCAT-3'	4 pmol
ubp1 MO	5'-TTGGGTCGGACAGGTACAATAATCC-3'	2-3 pmol

Full length *foxi1* cloning (3'- 5'):

Name	**Sequence**
Cla1-XLfoxi1-F	AAAAAAATCGATATGAGTGCATTTGATCCACAAGC
XLfoxi1-Sal1-R	AAAGTCGACTTATACTTCTGTACCTTCTCTG

foxi1.S reporter construct cloning and experiments:

To generate the *foxi1.S::gfp-utrophin* reporter construct, genomic DNA was prepared from *X. laevis* using the phenol/chloroform DNA purification (ThermoFisher #15593031 and associated protocol). A 2.7 kb fragment (Fig.S2D) of the *foxi1.S* promoter was cloned using Easy-A Hi-Fi Cloning Enzyme (Agilent #600404) and primers listed in the table below. The PCR fragment was ligated using the pGEM-T Easy Vector System

(Promega #A1360). The *foxi1.S* promoter sequence was subcloned into *a-tub::gfp-utrophin* (used in (Tasca et al., 2021)) after removal of the *a-tub* promoter sequence using HiFi DNA Assembly (NEB #E2621S) and Q5 High-Fidelity DNA Polymerase (NEB #M0491S) kits. *foxi1Δ1::gfp-utrophin* reporter version (Fig. S2C,D) was generated using Q5 High-Fidelity DNA Polymerase and primers listed in the table below. The *a-tub::mscarletI* reporter was generated by replacing the *gfp-utrophin* sequence in *a-tub::gfp-utrophin* by the *mscarletI* sequence using HiFi DNA Assembly and Q5 High-Fidelity DNA Polymerase and primers listed below. Final construct sequences were analyzed by whole-plasmid nanopore sequencing.

Cloning primers *foxi1.S* reporter (3'- 5'):

Name	**Sequence**
gDNA-Prom_foxi1_F	GCATAATGAATCCCAAGTGTACTG
gDNA-Prom_foxi1_R	GAAGCAATCGTTTAGAGACAGG
Foxi1prom_F	CGCTATTACGCCAGTCGACCGCATAATGAATCCCAAGTG
Foxi1prom_R	CAATTCGAATCGATGGGATCAGTTAAAGCTAGCAGGTC
MS2_rmATUB_F	GATCCCATCGATTCGAATTG
MS2_rmATUB_R	GGTCGACTGGCGTAATAG
Q5foxi1Del1_F	TCTGTAGCTGATGTCTATAATC
Q5foxi1Del1_R	TACCACTGTGTGACTCAG
MS2_rmGFPUtro_F	GTACAAGTAACCTCTAGAACTATAGTGAGTC
MS2_rmGFPUtro_R	TGCTCACCATGGTTTGGATCAATTCGAATC
mScarletI_F	GATCCAAACCATGGTGAGCAAGGGCGAG
mScarletI_R	GTTCTAGAGGTTACTTGTACAGCTCGTCCATG

Whole mount *in situ* hybridization and sections:

For antisense *in situ* hybridization probes, *slc26a4*, *slc4a1*, *ubp1* and *dmrt2* fragments were cloned from whole-embryo cDNAs derived from stages between 3 and 30 using primers listed below (ISH-primers). All sequences were verified by Sanger sequencing. In addition, the following, previously published probes were used: *foxi1* (Quigley et al., 2011), *foxj1* and *mcidas* (Stubbs et al., 2008; Stubbs et al., 2012), *foxa1* (Walentek et al., 2014), *tp63* (Haas et al., 2019), *atp6v1e1* (Walentek et al., 2015) and *dll1* (Tasca et al., 2021).

Embryos were fixed in MEMFA (100mM MOPS pH7.4, 2mM EGTA, 1mM MgSO4, 3.7% (v/v) Formaldehyde) overnight at 4°C and stored in 100% Ethanol at -20°C until used. DNAs were purified using the PureYield Midiprep kit (Promega #A2492) and were linearized before in vitro synthesis of anti-sense RNA probes using T7 or Sp6 polymerase (Promega, #P2077 and #P108G), RNAse inhibitor and dig-labeled rNTPs (Roche, #3359247910 and 11277057001). Embryos were in situ hybridized according to (Harland, 1991), bleached after staining with BM Purple (Roche #11442074001) and imaged. Sections were made after embedding in gelatin-albumin with Glutaraldehyde at 50-70µm as described in (Walentek et al., 2012).

Probe cloning primers (5'-3'):

Name	**Sequence**

ISH-dmrt2-F	CAAACCAGTGTATCAGAGAC
ISH-dmrt2-R	ACTCCTTTCCTAAGAAGCAG
ISH-ubp1-F	ATTCCTGAAGCAAGAAGACC
ISH-ubp1-R	GAGAATGTGAATCCCATGAG
ISH-slc26a4-F	GATTCATACCACCTATGACAC
ISH-slc26a4-R	TTCCAATAGTTCCCTAGATTCC
ISH-slc4a1-F	ATCTCCTATCTCACCTTTCAC
ISH-slc4a1-R	ATCCATCTGTCTGTCTTCTC
ISH-anti-GFP-F	ATGGTGAGCAAGGGCGAGG
ISH-anti-GFP-R	CTTGTACAGCTCGTCCATGCCATGCCGAGAGTG

Evaluation of WMISH staining and morphological evaluations:

Embryos were staged according to Nieuwkoop and Faber (1994) Normal Table of *Xenopus laevis* (Daudin). Garland Publishing Inc, New York ISBN 0-8153-1896-0. For the *foxi1* expression stage series wt embryos from multiple batches were mixed and at least 5 embryos per stage were assessed.

Images of embryos after *in situ* hybridization and corresponding sections were imaged using a Zeiss AxioZoom setup, Zeiss AxioImager.Z1 or Zeiss Stemi508 with Axiocam208-color, and images were adjusted for color balance, brightness and contrast using Adobe Photoshop.

In Fig.1B,C expression strength were categorized in normal, reduced, strongly reduced or increased. In Fig. 1D-G, 3C, S5B, expression level differences observed between the uninjected control sides and manipulated sides of embryos were scored in whole mount embryos, while depicted sections are shown for clarity. In Fig. 3A and S4C induction of expression was scored. In Fig. 3B *dll1* expression in the ventral epidermis was analyzed as normal or less (number of dots and expression intensity).

For analyses in Fig.2A and S2A, embryos injected with high dose of *foxi1* MO, cell morphology and cell size were evaluated for Fig. S2A (and delamination was confirmed in hemisected embryos) and skin lesions were evaluated for Fig. 2A.

Immunofluorescence staining and sample preparation:

Whole *Xenopus* embryos, were fixed at indicated stages in 4% paraformaldehyde at 4°C overnight or 2h at room temperature, then washed 3x 15min with PBS, 2x 30min in PBST (0.1% Triton X-100 in PBS), and were blocked in PBST-CAS (90% PBS containing 0.1% Triton X-100, 10% CAS Blocking; ThermoFischer #00-8120) for 30min-1h at RT. A detailed protocol was described in (Walentek, 2018).

Mouse anti-Acetylated-α-tubulin (Sigma/Merck #T6793) primary antibody (1:1000) was used to mark cilia / MCCs, Rabbit Anti-serotonin (Sigma/Merck #S5545) primary antibody (1:500) was used to mark SSCs applied at 4°C overnight. Secondary antibodies AlexaFlour-405-labeled goat anti-mouse (Invitrogen # A30104) and AlexaFlour 405-labeled goat anti-rabbit antibody (Invitrogen #A31556) were used for 2 h at RT (1:250). Antibodies were applied in 100% CAS Blocking (ThermoFischer #00-

8120). Actin was stained by incubation (30-120 min at room temperature) with AlexaFluor 405-labeled Phalloidin (1:800 in PBSt; Invitrogen #A30104), mucus-like compounds were stained by incubation (overnight at 4°C) with AlexaFluor-594- or -647-labeled or PNA (1:500-1000 in PBSt; Molecular Probes #L32459 and #L32460).

Fluorescence imaging, image processing and analysis:

Confocal imaging was conducted using either a Zeiss LSM880 or a Zeiss LSM980 microscope and Zeiss Zen software in the LIC and BiMiC imaging facilities. Confocal images were adjusted for channel brightness/contrast, Z-stack projections were generated and cell types were quantified based on their morphology using ImageJ (Schindelin et al., 2012). For analyses in Fig. 3D and S5A a detailed protocol for quantification of *Xenopus* epidermal cell type composition was published (Walentek, 2018).

For analysis and comparison of fluorescent reporter construct activity on confocal micrographs (Fig. 4A) in ImageJ, z-projections were performed using the “sum-slices” function. Induction of reporter expression in the endoderm (Fig. 4B) embryos were imaged using a Zeiss AxioImager.Z1 with Axiocam208-color camera. Induction was scored as positive when GFP fluorescence was detected in the vegetal half of the gastrula embryo. In some controls, activity was observed in involuting or animally positioned mesoderm, where maternal *foxi2* deposition occurs. Fluorescent intensities were color-coded using the function “lookup tables -> fire” (8 bit) in ImageJ.

RNA- and ATAC-sequencing on *Xenopus* mucociliary organoids and bioinformatics analysis:

Manipulations and bulk mRNA-seq used in this paper were generated and published here: (Brislinger-Engelhardt et al., 2023; Haas et al., 2019). scRNA-seq datasets were published here: (Aztekin et al., 2019; Briggs et al., 2018).

For Fig. 1A, data from (Brislinger-Engelhardt et al., 2023) were used, TPM values from .L and .S allo-allels were added, and the resulting matrix was clustered using Z-values per line and galaxy.eu (ggplot2_heatmap2/3.1.3.1+galaxy). For Fig. S1A-C, log2-fold changes were calculated using galaxy.eu (DeSeq2/2.1.3+galaxy) and visualized using (ggplot2_heatmap2/3.1.3.1+galaxy). For Fig. S1 D, the online tool associated with (Aztekin et al., 2019) was used (marionilab.cruk.cam.ac.uk/XenopusRegeneration). For Fig. S4B, the online tool associated with (Briggs et al., 2018) was used (kleintools.hms.harvard.edu/tools/currentDatasetsList_xenopus_v2.html) to extract lineage-enriched transcripts and the heatmap was generated using galaxy.eu (ggplot2_heatmap2/3.1.3.1+galaxy).

For ATAC-seq sample generation, injected and control embryos were cultured until st. 8. Animal caps were dissected in 1x Modified Barth’s solution (MBS) and transferred to 0.5x MBS + Gentamycin (Sive et al., 2007a). 2 organoids per condition and replicate were collected in PBS and ATAC-seq was performed as described in (Buenrostro et al., 2013; Esmaeili et al., 2020). In short: Embryos were injected bilaterally in the animal

hemisphere at the two-cell stage with 3pmol *foxi1* MO or remained uninjected, animal caps were prepared at st. 8, and organoids were collected upon the appearance of the dorsal lip in control embryos cultured in parallel to the organoids (st. 10). Organoids were transferred from MBS plates into a 1.5 mL low-bind microcentrifuge tube (Eppendorf #0030108051) containing 1 mL of ice-cold 1x PBS. Samples were spun at 500 g at 4 ºC in the centrifuge for five minutes before removing the PBS and repeating the wash step with fresh ice-cold 1x PBS. 50 µL of ice-cold lysis buffer (10 mM Tris pH 7.4, 10 mM NaCl, 3 mM MgCl2, 0.1% (w/v) Igepal CA-630) and pipetted to break up samples. Samples were centrifuged at 500 g for 10 min at 4 ºC and pellets were resuspended in 25 µL TD Buffer, 2.5 µL TDE1 Enzyme and 22.5 µL Nuclease-Free water (Illumina #20034198). Samples were pelleted to mix and incubated on a ThermoMixer at 37 ºC, 700 rpm for 30 min. Following incubation, the samples were cleaned with MinElute Reaction Cleanup Kit (Qiagen, #28204), following manufacturer instructions and eluted into 11 µL Buffer EB.

Libraries were prepared in collaboration with the NIG, University Medical Center Göttingen. Quality was assessed with the Agilent Fragment Analyzer and prepared with the ATAC-seq Kit (Active Motif, #53150). Samples were sequenced in triplicate on an Illumina NovaSeq6000 with 150 nucleotide paired-end reads, totaling 50 million reads per sample.
Raw sequencing files were assessed for quality using FastQC (v0.11.9, Andrews, S. FastQC A Quality Control tool for High Throughput Sequence Data. http://www.bioinformatics.babraham.ac.uk/projects/fastqc/), and adapter sequences were removed with TrimGalore (v0.6.7, https://doi.org/10.5281/zenodo.7598955). Data were aligned to the *X. laevis* genome assembly v9.2 using BWA-MEM (v0.7.17, https://arxiv.org/abs/1303.3997). Mitochondrial reads were removed using Samtools (v1.21) (Danecek et al., 2021), and peak calling was performed with the callpeak function of MACS2 (v2.2.7.1) (Feng et al., 2012). Differential analysis was performed with the bdgdiff function of MACS2 and Venn diagrams were generated with VennDiagram v1.7.3 in R v4.4.1. Heatmaps showing the average ATAC-seq signal were generated using deepTools (v3.5.4) (Ramírez et al., 2016). Peaks were annotated for the nearest *X. laevis* gene and transcription factor binding motifs with Homer (v4.11) (Heinz et al., 2010), Plant-specific transcription factors were manually excluded from the lists of transcription factors.. Bioinformatic analyses were performed on the Galaxy / Europe platform (usegalaxy.eu) (Community, 2024). ATAC-seq data generated for this study was deposited at NCBI GEO under (#pending).

<u>Quantification and statistical evaluation:</u>
Stacked bar graphs were generated in Microsoft Excel. Heatmaps and Venn diagrams were generated using the Galaxy Europe platform (usegalaxy.eu) and R.
Sample sizes for all experiments were chosen based on previous experience and used embryos derived from at least two different females. No randomization or blinding was applied.

<u>Use of shared controls:</u>

For some of the *in situ* and IF experiments shared controls were used in multiple graphs; all experiments are listed in the supplemental experiment log.

Figure legends:

Figure 1: Foxi1, Ubp1 and Dmrt2 differentially regulate ionocyte development
(A) Temporal expression analysis of core ISC genes. Heatmap of line-normalized z-scores of TPMs (transcripts per million reads) derived from mRNA-seq of *Xenopus* mucociliary organoids over the course of development (st. 9 - 32). **(B-G)** Knockdown of ISC transcription factors (*foxi1* MO, *ubp1* MO, *dmrt2* MO) and analysis of effects by WMISH at st. 29 - 32 against *atpv1e1* and *foxi1* (pan-ISC markers), *ubp1* and *slc25a4/pendrin* (β-ISC markets), and *dmrt2* and *slc4a1/ae1* (α-ISC markers). Representative images **(B,D,E,G)** and quantification **(C, F, H)** of results. n = number of embryos analyzed per condition. Rescues (co-injection of *foxi1* mRNA) depicted in **(B,C)** were scored as normal (norm.), reduced (red.), strongly reduced (s.red.) and increased (incr.). Color code is shown in **(B)**. In conditions depicted in **(D, E, G)**, expression levels were scored as less, more or equal expression as compared to the uninjected control side. Color code is shown in **(F)**.

Figure 2: Foxi1 acts in a concentration-dependent manner to specify multipotent progenitors
(A) Immunofluorescence confocal micrographs (IF) from control (ctrl.) and *foxi1* morphants (*foxi1* MO; low concentration) at st. 32 stained for Acetylated-α-tubulin (Ac.-α-tub., cilia, grey), F-actin (Actin, cell borders and morphology, grey), and mucus (PNA, magenta). Targeted cells were identified by membrane GFP expression (memGFP, green). Location of insets is indicated by dashed yellow box in upper panels.

Quantification of cell type composition is depicted as pie-charts, goblet cells (blue), ISCs (yellow), MCCs (green) and SSCs (red). n embryos (above chart) and n quantified cells (in/left of chart). **(B)** Brightfield images and quantification of st. 30-32 embryos. Uninjected controls (ctrl.), *foxi1* morphants (*foxi1* MO; high concentration) and morphants co-injected with *foxi1* mRNA (rescue) are depicted. Skin lesions (dashed yellow outline) were quantified. **(C,D,E)** Analysis of *foxi1::gfp-utrophin* reporter (green) injected embryos by IF **(C,E)** and WMISH against *gfp* **(D)**. **(C)** IF for Acetylated-α-tubulin (Ac.-α-tub., cilia, grey), F-actin (Actin, cell borders and morphology, grey), and serotonin (SSCs, grey) at st. 32. Targeted cells were identified by nuclear RFP expression (H2B-RFP, blue). Magnifications of intercalating GFP(+) cell types are shown in insets. Location of insets is indicated by dashed yellow boxes in left panels. **(D)** Sections of epidermal locations from embryos depicted in Fig. S3C show *gfp* expressing cells in the epidermis at key stages of mucociliary development (st. 10, 16, 25, 32). **(E)** IF for *foxi1::gfp-utrophin* reporter (green) and F-actin (Actin, cell borders and morphology, magenta) at st. 10.5 - 32 on hemistected embryos. Targeted cells were identified by membrane RFP expression (mRFP, grey). Additional stages and full images shown in Fig. S4A.

Figure 3: Foxi1 induces and Ubp1 terminates Notch ligand expression

(A,B,C) Manipulation of mucociliary cell fate transcription factors *foxi1* and *ubp1* (ISCs/MPPs), *mcidas* and *foxj1* (MCCs), *foxa1* (SSCs) and *ΔN-tp63* (basal cells) and analysis of effects by WMISH at st. 9 **(A)**, st. 11 **(B)** and st. 16 **(C)** against *dll1* (Notch ligand) and *foxi1* (MPP/ISC marker). **(A)** Representative images of control (ctrl.) and manipulated embryos (animal views) after mRNA overexpression of transcription factors to test premature induction of *dll1*. Quantification of results and effects on *dlc* are shown in Fig. S4C. Embryos were scored as induced or non-induced expression. **(B)** Representative images of control (ctrl.) and *foxi1* morphants (*foxi1* MO) (ventral views) to test effects on *dll1* expression. Quantification of results is shown in lower panel. Locations of insets are indicated by dashed yellow box in upper panels. Embryos were scored as normal or reduced (less) expression of *dll1*. **(C)** Representative images of section embryos after unilateral knockdown of *ubp1* (*ubp1* MO). Expression of markers was scored as more, less or equal to uninjected control (ctrl.) side. Locations of insets are indicated by dashed yellow box in left panels. **(D)** IF of control (ctrl.) and *ubp1* morphants (*ubp1* MO) at st. 32 stained for Acetylated-α-tubulin (Ac.-α-tub., cilia, grey), F-actin (Actin, cell borders and morphology, grey), and mucus (PNA, magenta). Targeted cells were identified by membrane GFP expression (memGFP, green). Location of insets is indicated by dashed yellow box in upper panels. Quantification of cell type composition is depicted as pie-charts, goblet cells (blue), ISCs (yellow), MCCs (green) and SSCs (red). n embryos (above chart) and n quantified cells (in/left of chart).

Figure 4: Foxi1 regulates its own expression

(A) IF of embryos injected with *foxi1::gfp-utrophin* or *foxi1Δ1::gfp-utrophin* reporters (green) at st. 32 stained for Acetylated-α-tubulin (Ac.-α-tub., cilia, grey), F-actin (Actin, cell borders and morphology, grey), and serotonin (SSCs, grey) at st. 32. Targeted cells

were identified by nuclear RFP expression (H2B-RFP, blue). Right panels show false-color of GFP fluorescence intensity. **(B)** Brightfield and epifluorescence images of hemisected st. 11 gastrula embryos injected vegetally with *foxi1::gfp-utrophin* (green), membrane RFP (memRFP; magenta) as control (*memRFP*) or with additional co-injection of *foxi1* mRNA (*foxi1* + *memRFP*). Right panels show false-color of GFP fluorescence intensity. Induction was scored as positive when GFP was detected in areas below the equator (mesendoderm). Ctrl. n = 7 induced, 26 non-induced; *foxi1* mRNA = 26 induced, 11 non-induced.

Figure 5: Foxi1 regulates mucociliary epidermal competence through epigenetic means

(A) Profiles of ATAC-Seq normalized accessibility around peak center ±1 kb in controls (ctrl.) and foxi1 morphant (*foxi1*MO) organoids. (**B)** Venn diagram of peaks present in uninjected organoids (grey) and *foxi1* MO-injected organoids (purple). (**C)** Top 15 transcription factor binding motifs predicted in sets of peaks with lost, maintained or gained accessibility after *foxi1* MO. **(D)** Distribution of accessible regions around epidermal genes *krt12.4* and *dll1.* Lost, maintained and gained tracks as generated by MACS2 bdgdiff analysis and visualized in IGV. Turquoise track = control (ctrl.) and purple track = morphant (*foxi1* MO). n = 2 organoids per condition and replicate. 3 replicates.

Figure S1: Notch regulation of ISC genes and ISC-subtype markers

(A,B,C) Effects of Notch gain (*nicd*; **A**), Notch loss (*suh-dbm*; **B**) and Notch and MCC loss (*suh-dbm* + *dn-mcidas*; **C**) on core ISC gene expression in key developmental stages (st. 10, 16, 25, 32). Heatmaps depict log2-fold change values derived from DEseq2. Asterisks indicate statistical significant (adj-p value < 0.05) changes. **(D)** Boxplots of ISC gene expression from scRNA-seq data published in Aztekin et al., 2019. Visualization was generated using the published online tool: marionilab.cruk.cam.ac.uk/XenopusRegeneration.

Figure S2: Early Foxi1 functions, expression and reporter construct

(A) Representative brightfield images of controls (ctrl.) and embryos (animal views) after *foxi1* MO (*foxi1*MO; high concentration) injection at st. 8. Morphants showed enlarged cells and delamination of animal cells into the blastocoel. Quantification of results shown in the right graph. Delamination events were scored based on morphological analysis. n = number of embryos. **(B)** WMISH expression analysis of *foxi1* across mucociliary epidermis development stages (st. 9 - 32). St. 9, 10 = animal views; st. 12, 16 = ventral views; st. 25, 32 = lateral views. Bottom row panels = magnified views of epidermal areas. **(C,D)** Generation and promoter sequences of *foxi1::gfp-utrophin* or *foxi1Δ1::gfp-utrophin* reporters. **(C)** Schematic representation of cloned genomic *foxi1.S* promoter locus (grey box) and position of Foxi2 binding region determined in Cha et al., 2012 (black outlined box). **(D)** Promoter sequence with indicated predicted core Foxi binding-motifs (yellow) and Foxi2 binding region (bold, underscored).

Figure S3: Characterization of the foxi1 reporter

(A,B) IF of embryos injected with *foxi1::gfp-utrophin* (green) and α-tub.::mscarletI (magenta) reporters at st. 32 stained for Acetylated-α-tubulin (Ac.-α-tub., cilia, grey), F-actin (Actin, cell borders and morphology, grey), and serotonin (SSCs, grey) in **(A)**; or for Acetylated-α-tubulin (Ac.-α-tub., cilia, grey) and F-actin (Actin, cell borders and morphology, grey), in **(B)**. In **(B)** targeted cells were identified by nuclear RFP expression (H2B-RFP, magenta). **(C)** WMISH expression analysis of *foxi1::gfp-utrophin* (stained for *gfp* transcripts) across mucociliary epidermis development stages (st. 9 - 32). St. 9, 10 = animal views; st. 12, 16 = ventral views; st. 25, 32 = lateral views. Bottom row panels = magnified views of epidermal areas. Related to sections shown in Fig. 2D.

Figure S4: Foxi1 expression in mucociliary development and Notch ligand induction

(A) IF for *foxi1::gfp-utrophin* reporter (green) and F-actin (Actin, cell borders and morphology, magenta) at st. 10.5 - 32 on hemistected embryos. Targeted cells were identified by membrane RFP expression (mRFP, grey). Related to sections shown in Fig. 2E. **(B)** Heatmap of mucociliary marker gene enrichment differentiation inlneages from scRNA-seq data published in Briggs et al., 2018. Values were derived using the published online tool: kleintools.hms.harvard.edu/tools/currentDatasetsList_xenopus_v2.html. NNE = non-neural ectodermal precursors; BC – basal cells; ISC = ionocytes; MCC = multiciliated cells; SSC = small secretory cells; GB = outer-layer goblet cells. **(C)** Representative images of st. 9 control (ctrl.) and manipulated embryos (animal views) after mRNA overexpression of transcription factors to test premature induction of *dlc*. Quantification of results and effects on *dll1* (yellow) and *dlc* (blue) graphs. Embryos were scored as induced or non-induced expression. Related to Fig. 3A.

Figure S5: Effects of Notch manipulation of mucociliary development

(A) IF of control (ctrl.), *dll1* (*dll1* MO) and *notch1* (*notch1* MO) morphants and morphants after Notch gain of function (co-injected with *nicd*) at st. 32 stained for Acetylated-α-tubulin (Ac.-α-tub., cilia, grey), F-actin (Actin, cell borders and morphology, grey), and mucus (PNA, magenta). Targeted cells were identified by membrane GFP expression (memGFP, green). Quantification of cell type composition is depicted as pie-charts, goblet cells (blue), ISCs (yellow), MCCs (green) and SSCs (red). n embryos (above chart) and n quantified cells (in/left of chart). **(B)** WMISH for cell type markers (*foxi1* = ISC; *foxj1* = MCCs; *foxa1* = SSCs; basal cells = *ΔN-tp63*) at st. 16/17 in controls and after knockdown of *dll1* (*dll1* MO). + = low dose, ++ = medium dose, +++ = high dose. Sections of embryos allow detailed comparison between injected (*dll1* MO) and uninjected control (ctrl.) sides of embryos. Graphs: Quantification of results. Expression levels were scored more, equal, less expression on the injected vs. uninjected sides. n = number of embryos.

Figure S6: Foxi1 is required for genomic accessibility of mucociliary genes
(A-D) Distribution of accessible regions around genes required for development and cell fates specification in the embryonic mucociliary epidermis of *Xenopus*. Lost, maintained and gained tracks as generated by MACS2 bdgdiff analysis and visualized in IGV. **(A)** *ubp1.L;* **(B)** *dmrt2.S;* **(C)** *foxj1.L;* and **(D)** *tp63.L.* Turquoise track = control (ctrl.) and purple track = morphant (*foxi1* MO). n = 2 organoids per condition and replicate. 3 replicates.

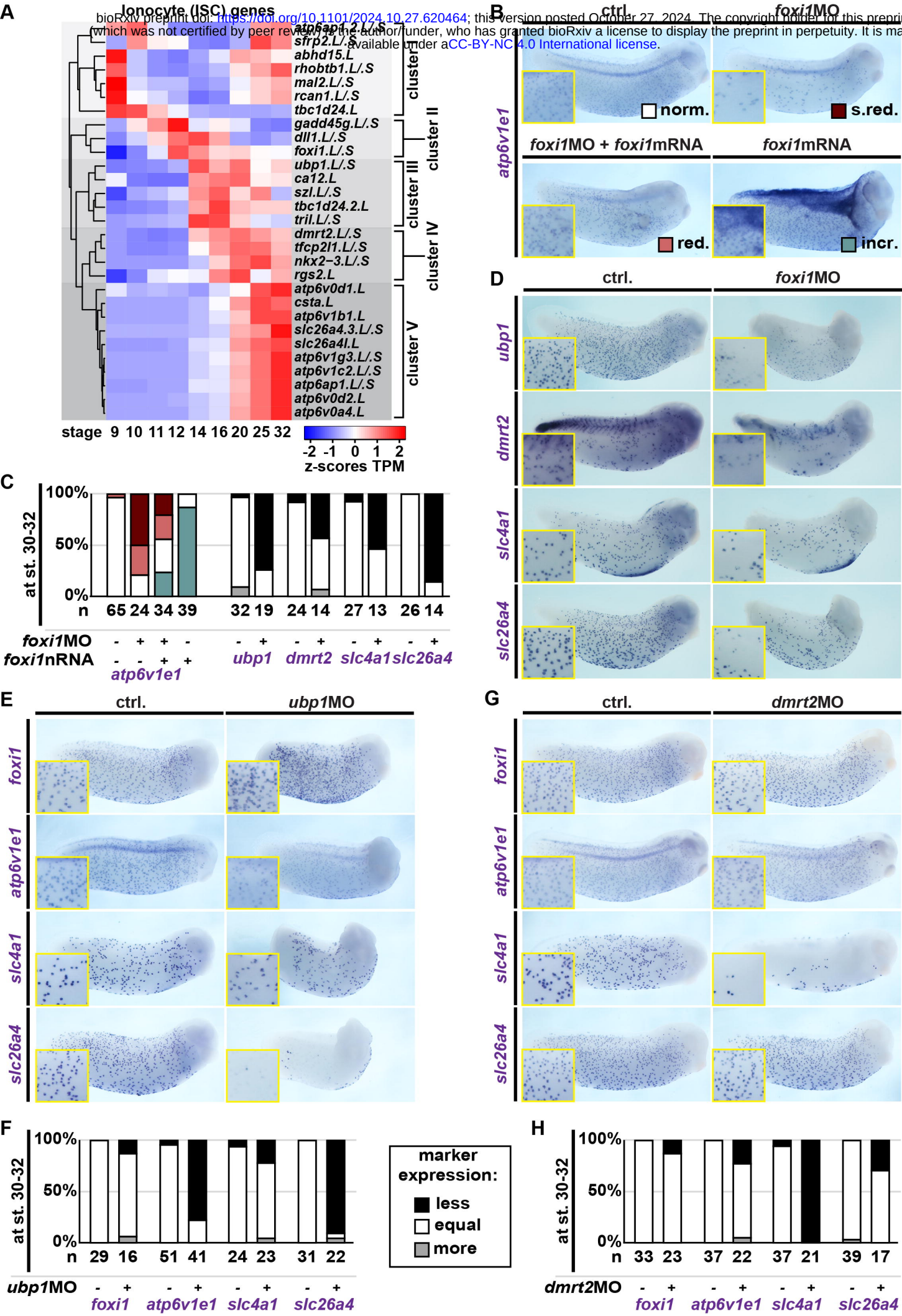

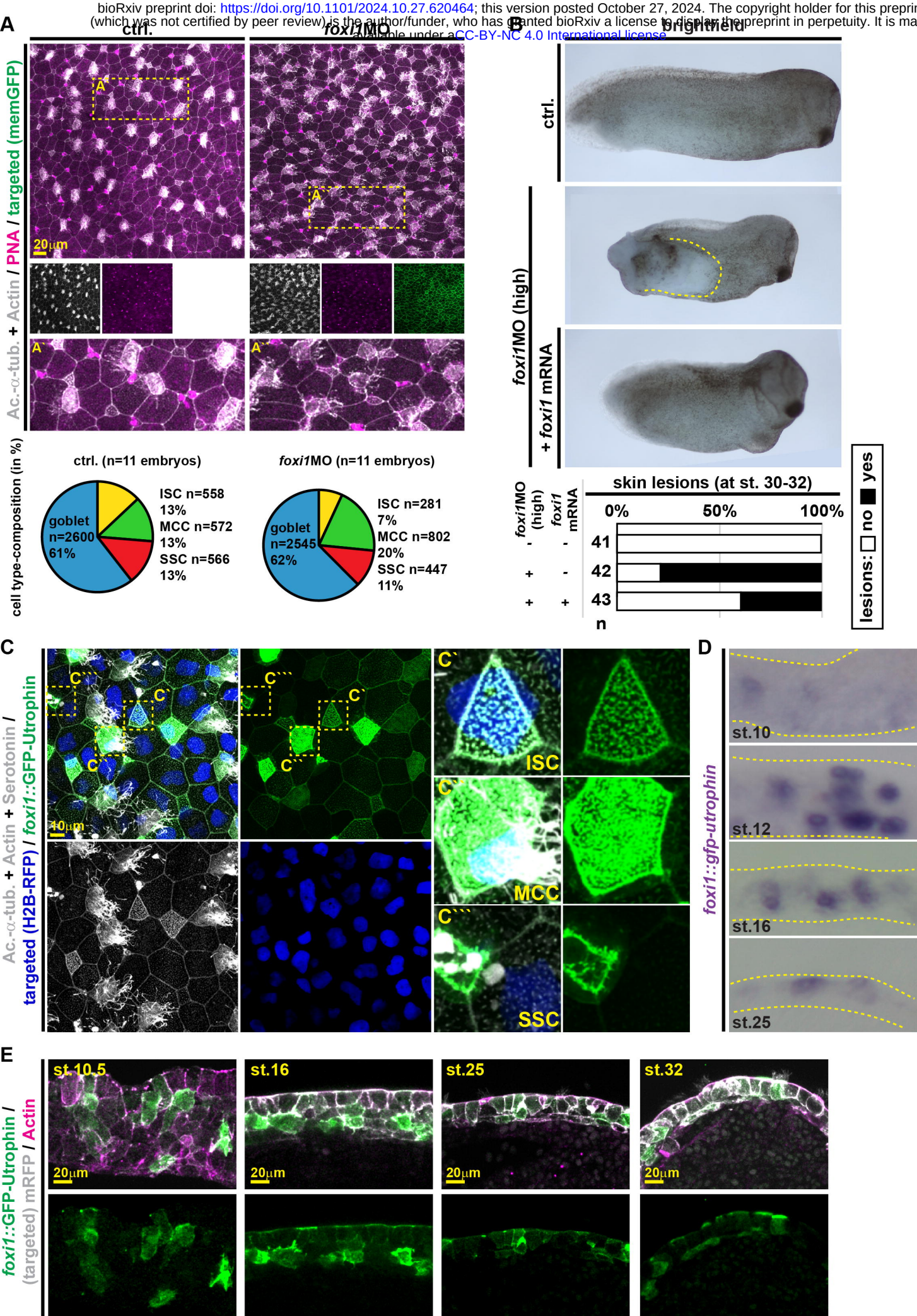

Bowden, Brislinger, Hansen et al. Figure 3

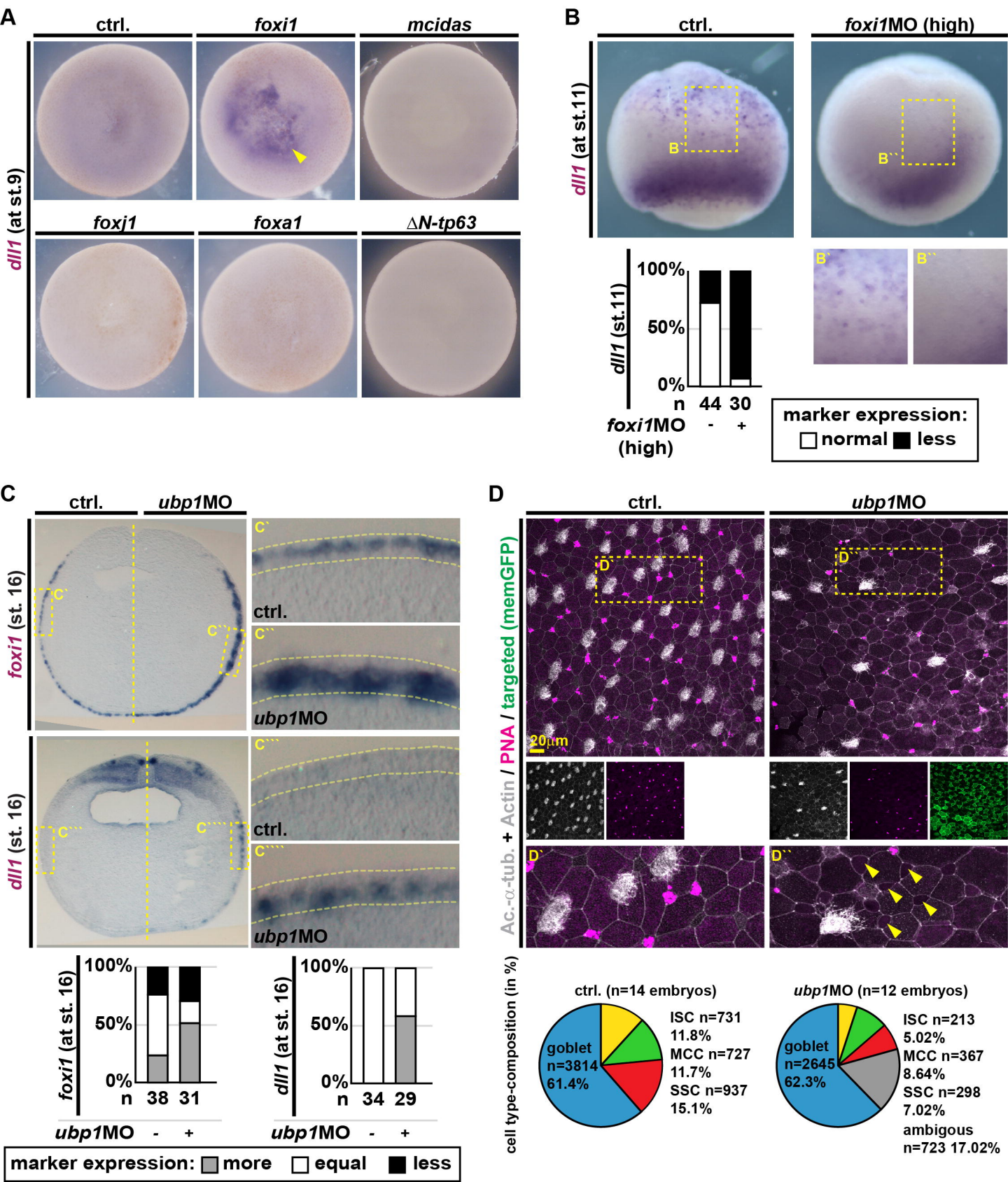

Bowden, Brislinger, Hansen et al. Figure 4

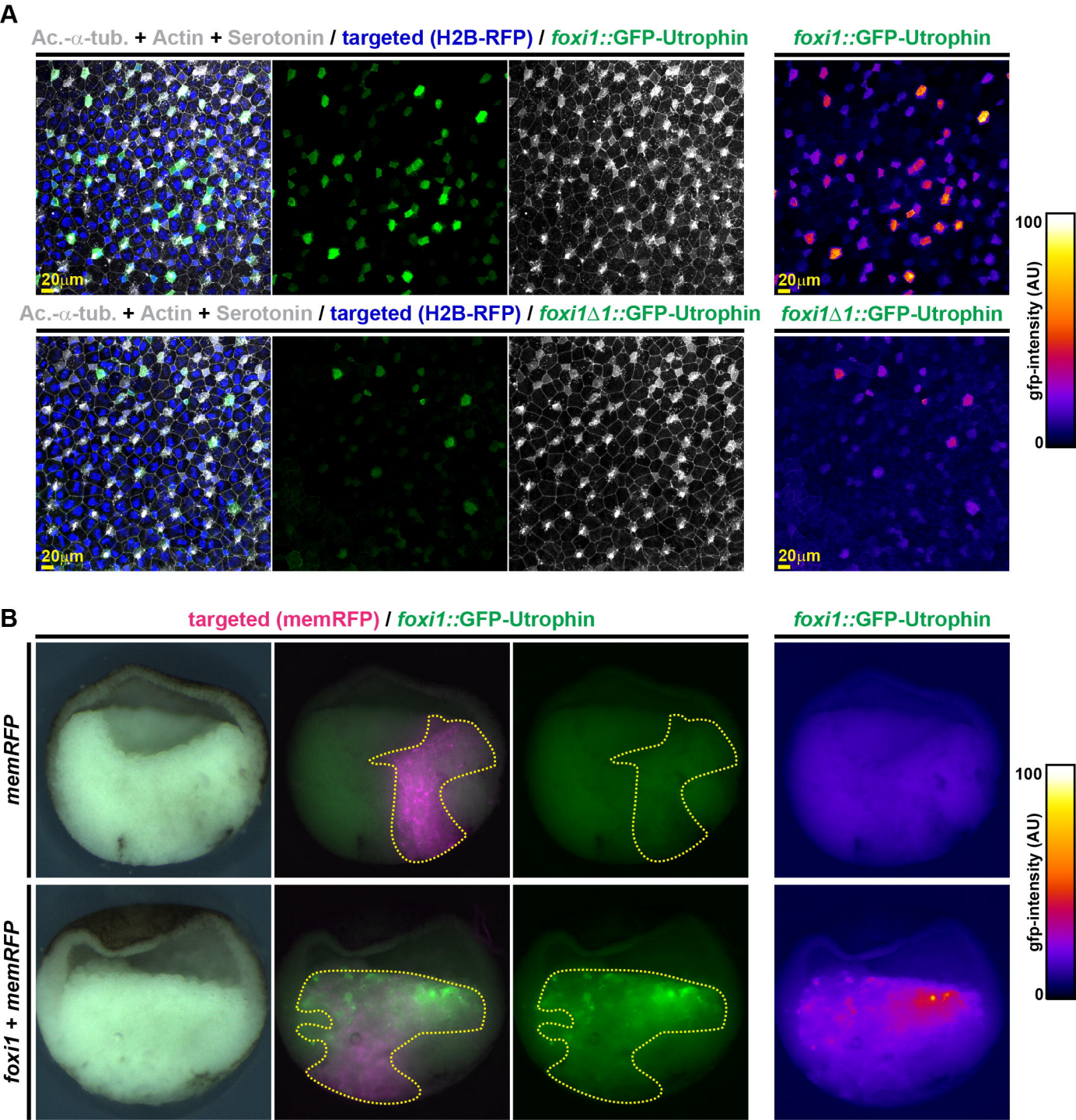

Bowden, Brislinger, Hansen et al. Figure 5